

Cavity-modified quantum electron transport in multi-terminal devices and interferometers

Dalin Boriçi, Geva Arwas, and Cristiano Ciuti

Université Paris Cité, CNRS, Matériaux et Phénomènes Quantiques, 75013 Paris, France

(Dated: December 10, 2024)

We theoretically investigate transport affected by cavity-mediated electron hopping in multi-terminal quantum Hall bars, quantum point contacts, and Aharonov-Bohm interferometers. Beyond determining conductances and resistances, we analyze spatially resolved current distributions and local density of states. Our study reveals how cavity-mediated inter-edge scattering impacts quantum magnetotransport in finite-size systems and how the cavity-mediated hopping significantly alters electron quantum interference effects.

I. INTRODUCTION

The effects of vacuum field fluctuations in condensed matter systems, previously considered negligible due to their minimal influence in free space, have recently garnered significant attention [1–3]. Advances in the fabrication of electromagnetic cavities, which enable exceptionally strong photon mode confinement [4–7], have brought ultra-strong light-matter coupling [8, 9] into the realm of feasibility. This has transformed these previously overlooked interactions into a vibrant research area, as they are now recognized for their profound impact on modifying and controlling quantum phases of matter.

On the theoretical front, models have been developed to explore these effects on superconductivity [10–14], topology [13, 15–28], and transport [21, 29–34]. Experimentally, recent attention has been directed towards magneto-transport properties and quantum Hall systems [35–40], as well as the influence on the critical temperature of charge density wave transitions [41].

In a recent theoretical study [32], we developed a framework for quantum electron transport influenced by cavity vacuum fields, focusing on a regime where photon degrees of freedom can be adiabatically eliminated. This work introduced an effective single-electron Hamiltonian that incorporates cavity-mediated electron hopping [16]. Within this framework, we used the Landauer-Büttiker formalism [42] to compute the conductance of one-dimensional systems and two-terminal quantum Hall systems. This emerging field, still in its infancy, holds significant potential for application to a broad range of mesoscopic quantum systems. In this paper, we extend the framework to multi-terminal devices, enabling the investigation of cavity-modified spatially-resolved current fields and local density of states. These advancements provide a deeper understanding of microscopic transport phenomena in complex quantum systems. Specifically, we examine the role of cavity vacuum fields in multi-terminal quantum Hall bars and quantum point contacts, which have been studied experimentally [36, 37], and predict cavity-induced modifications in Aharonov-Bohm interferometers, a system yet to be explored experimentally.

II. THEORETICAL FRAMEWORK

Let \hat{H}_0 be a single-electron tight-binding Hamiltonian, whose states $\{|i\rangle\}_{i \in \text{sites}}$, localized on the lattice sites, form an orthonormal basis for the single-electron Hilbert space. Let t_{ij} denote the hopping coupling between sites i and j , and let \hat{d}_i^\dagger be the fermion creation operator such that $\hat{d}_i^\dagger|\text{vac}\rangle = |i\rangle$, where $|\text{vac}\rangle$ is the vacuum state.

In a single-mode approximation, the cavity field vector potential can be expressed as $\hat{\mathbf{A}}(\mathbf{r}) = \mathbf{A}_{\text{vac}}(\mathbf{r})(\hat{a} + \hat{a}^\dagger)$, where $\mathbf{A}_{\text{vac}}(\mathbf{r})$ is the spatial profile of the mode, and \hat{a}^\dagger and \hat{a} are the photonic mode creation and annihilation operators. Light-matter coupling is introduced via the Peierls substitution, where the Peierls phase operator is $\hat{\phi}_{ij} = (\hat{a} + \hat{a}^\dagger)g_{ij}$, with $g_{ij} = -\frac{e}{\hbar} \int_{\mathbf{r}_i}^{\mathbf{r}_j} d\mathbf{r} \cdot \mathbf{A}_{\text{vac}}(\mathbf{r})$.

Following [32], expanding the Peierls factors $e^{i\hat{\phi}_{ij}}$ to first order in g_{ij} , we obtain a paramagnetic coupling proportional to $(\hat{a} + \hat{a}^\dagger)$. This coupling is treated as a perturbation on \hat{H}_0 using the intermediate Hamiltonian technique [43]. The resulting effective Hamiltonian projected onto the zero-photon subspace is $\hat{H}_{\text{eff}} = \hat{H}_0 + \hat{\Gamma}$, with

$$\hat{\Gamma} = \sum_{\lambda\lambda'} \Gamma_{\lambda\lambda'} \hat{c}_\lambda^\dagger \hat{c}_{\lambda'}.$$

Here, \hat{c}_λ^\dagger and \hat{c}_λ are the creation and annihilation operators for the single-particle eigenstates. Using such basis, the bare Hamiltonian can be written in the diagonalized form

$$\hat{H}_0 = \sum_{\lambda} \varepsilon_{\lambda} \hat{c}_{\lambda}^{\dagger} \hat{c}_{\lambda},$$

where $\hat{c}_\lambda^\dagger|\text{vac}\rangle = |\phi_\lambda\rangle = \sum_i \phi_\lambda(i)|i\rangle$. The cavity-mediated hopping coupling between single-particle eigenstates reads:

$$\Gamma_{\lambda\lambda'} = - \sum_{\mu} \left(\frac{\text{sgn}[\varepsilon_{\mu} - \min(\varepsilon_{\lambda}, \varepsilon_{\lambda'})]}{|\varepsilon_{\mu} - \frac{\varepsilon_{\lambda} + \varepsilon_{\lambda'}}{2}| + \hbar\omega_{\text{cav}}} \right) h_{\lambda\mu} h_{\mu\lambda'}, \quad (1)$$

where $h_{\alpha\beta} = \sum_{ij} (-ig_{ij}t_{ij})\phi_{\alpha}^*(i)\phi_{\beta}(j)$.

Note that the $\hat{\Gamma}$ matrix effectively couples electrons injected near the Fermi energy E_F [32], which is what

matters for transport in linear-response regime (limit of vanishing applied voltages).

The effective Hamiltonian can be written in the initial tight-binding basis as

$$\hat{H}_{\text{eff}} = \sum_{ij} \tilde{t}_{ij} \hat{d}_i^\dagger \hat{d}_j,$$

where \tilde{t}_{ij} represents the cavity-mediated hopping coupling (for $i \neq j$) and on-site energy shift (for $i = j$). In a nearest-neighbor tight-binding lattice, we will have for non-neighboring sites $t_{ij} = 0$, but instead $\tilde{t}_{ij} \neq 0$. This formalism can account for continuous systems in the limit where the lattice spacing is small enough. In what follows, we generalize the framework described in [32] by considering multi-terminal configurations, local density of states, and spatially-dependent current densities.

A. Multi-terminal linear-regime transport

Throughout this article, we shall examine the responsive behavior of devices by driving current through the electrodes they are coupled to. The Landauer-Büttiker formalism is a powerful tool that relates current and voltage drops across the leads (electrodes) through the scatterer's conductance (or equivalently, resistance) [44, 45]. We provide a brief outline of this formalism here, as it will be instrumental later in discussing driving currents and voltage biases interchangeably.

Consider a scattering device connected to N_L leads. In Landauer-Büttiker formalism, we can obtain the current I_p flowing through lead p via $I_p = \sum_{q=1}^{N_L} G_{pq}(V_p - V_q)$, with $(V_p - V_q)$ being the voltage drop between leads p and q and G_{pq} the linear conductance matrix, an intrinsic property of the device. Such a matrix is obtained by either solving the scattering problem, or equivalently by using the non equilibrium Green's functions (NEGF) formalism [46], which we discuss in Sec. II B. The conductance matrix obeys the following property $\sum_p G_{pq} = \sum_k G_{qk}$ for all q , essentially ensuring Kirchoff's law $\sum_p I_p = 0$. Defining $\tilde{G}_{pq} = -G_{pq} + \delta_{pq} \sum_{k=1}^{N_L} G_{pk}$, the Landauer Büttiker formula can be re-expressed as:

$$I_p = \sum_{q=1}^{N_L} \tilde{G}_{pq} V_q. \quad (2)$$

The \tilde{G} matrix is singular and its kernel is of dimension one, since $\sum_p \tilde{G}_{pq} = \sum_q \tilde{G}_{pq} = 0$. The voltages are defined with respect to an origin (ground voltage). By setting $V_{N_L} = 0$, the matrix equation reduces to $I_p = \sum_{q=1}^{N_L-1} \tilde{G}_{pq} V_q$ for $p \in \{1, \dots, N_L - 1\}$. Removing the last row and line from \tilde{G} , we obtain the reduced invertible $(N_L - 1)$ -dimensional square matrix \mathcal{G} , so we can write the voltages in terms of the imposed currents using

the resistance matrix $\mathcal{R} = \mathcal{G}^{-1}$. This can be written as

$$V_q = \sum_{p=1}^{N_L-1} \mathcal{R}_{qp} I_p, \quad (3)$$

for $q \in \{1, \dots, N_L - 1\}$.

B. Conductance matrix and local density of states

At a given Fermi energy E_F (we are considering the zero temperature limit), the linear conductance matrix [42] is given by the Caroli formula:

$$G_{pq}(E_F) = \frac{e^2}{h} \text{Tr}\{G^r \Gamma_p G^a \Gamma_q\}. \quad (4)$$

The quantities involved are the following: the retarded $G^r(E) = (E - \hat{H}_{\text{eff}} - \Sigma^r)^{-1}$ and advanced $G^a = (G^r)^\dagger$ Green's functions of the device coupled to the leads and the linewidths associated to each lead, namely $\Gamma_q = i(\Sigma_q^r - \Sigma_q^a)$. The self-energies due to the individual leads are given by $\Sigma_q^r = \tau_q^\dagger g_q^r \tau_q$. Here, the τ_q^\dagger are the coupling matrices of the scattering device to the leads, while g_q^r is the retarded Green's function of the isolated infinite lead, which we do not need to compute entirely (see Appendix A on how to obtain the lead's self-energy). The full self-energy is given by the sum $\Sigma^r = \sum_q \Sigma_q^r$, since the leads are considered independent. The retarded Green's functions contain all the information about the spectrum of the system. In particular, the electron spectral function is given by $A = -\frac{1}{\pi} \Im\{G^r\}$. From there, we can extract the density of states, that is the trace of A , or the local density of states, given by $\rho(\mathbf{r}) = -\frac{1}{\pi} \Im\{\langle \mathbf{r} | G^r | \mathbf{r} \rangle\}$. The ^r superscript stands for retarded, whilst ^a for advanced. Both are related to one another through hermitian conjugation.

C. Spatially-dependent current densities

Here, we derive the averaged non-equilibrium current density. We follow a derivation similar in fashion to the one carried out for bond currents in Ref. [47]. The main difference is that we derive the current vector for arbitrary long-range hopping and multi-terminal configurations. With our tight-binding effective Hamiltonian $\hat{H}_{\text{eff}} = \sum_{ij} \tilde{t}_{ij} \hat{d}_i^\dagger \hat{d}_j$, we can define a velocity operator $\hat{\mathbf{v}} = i/\hbar [\hat{H}_{\text{eff}}, \hat{\mathbf{r}}]$, with $\hat{\mathbf{r}} = \sum_j \mathbf{r}_j |j\rangle \langle j|$. The electronic charge density operator is given by $\hat{n}(\mathbf{r}_j) = -e/\mathcal{V}_{\text{cell}} |j\rangle \langle j|$, and the current density operator by $\hat{\mathbf{j}}(\mathbf{r}_k) = \frac{1}{2} [\hat{n}(\mathbf{r}_k) \hat{\mathbf{v}} + \hat{\mathbf{v}} \hat{n}(\mathbf{r}_k)]$, where $\mathcal{V}_{\text{cell}}$ is the volume of the lattice elementary cell. In second quantization, the current operator reads:

$$\hat{\mathbf{j}}(\mathbf{r}_k) = -i \frac{e}{2\mathcal{V}_{\text{cell}}} \sum_j (\mathbf{r}_j - \mathbf{r}_k) \left(\tilde{t}_{kj} \hat{d}_k^\dagger \hat{d}_j - \tilde{t}_{jk} \hat{d}_j^\dagger \hat{d}_k \right). \quad (5)$$

We note in passing, that in the standard case of tight-binding lattice with only near-neighbor hopping, where $t = \hbar^2/(2m_*a^2)$, taking the continuum limit would yield the well known continuum result $\hat{j}(\mathbf{r}) = -e\frac{\hbar}{m_*}\mathfrak{S}\{\hat{\psi}^\dagger(\mathbf{r})\nabla\hat{\psi}(\mathbf{r})\}$, with $\hat{\psi}^\dagger(\mathbf{r})$ being the electron field operator. For a system in thermal equilibrium, it is convenient to introduce the lesser Green's functions: $G_{ij}^<(t-t') = \frac{i}{\hbar}\langle\hat{c}_j^\dagger(t')\hat{c}_i(t)\rangle = \frac{1}{2\pi\hbar}\int_{\mathbb{R}}dEe^{-\frac{i}{\hbar}(t-t')E}G_{ij}^<(E)$. The averaged current operator in the steady state can be expressed as:

$$\mathbf{j}(\mathbf{r}_k) = \frac{e}{\mathcal{V}_{\text{cell}}\hbar}\sum_j(\mathbf{r}_j - \mathbf{r}_k)\int_{\mathbb{R}}dE\mathfrak{S}\{\tilde{t}_{kj}G_{jk}^<(E)\}. \quad (6)$$

We can account for the leads using the Keldysh equation in its matrix form $G^<(E) = G^r(E)\Sigma^<(E)G^a(E)$ and the relation giving the lesser self-energy in terms of the linewidths, namely $\Sigma^<(E) = \sum_{q=1}^{N_L}f(E - \mu_q)\Gamma_q(E)$ [47, 48], with $f(x) = 1/(e^{\beta x} + 1)$ the Fermi-Dirac distribution. In the zero temperature limit ($\beta \rightarrow +\infty$), $f(x) = \Theta(-x)$, the Heaviside step function. Let us assume the voltage drops among the different leads are small with respect to the all relevant spectrum energy gaps (i.e. the Green's functions are slowly varying over the energy scale related to the voltages), which is the case in the linear response regime. In these conditions, we can define a Fermi energy as $E_F = \sum_q\mu_q/N_L$ and voltages as $eV_q = \mu_q - E_F$. We split the integral by integrating first up to E_F and then for each lead q from E_F to μ_q . Since the eV_q are considered as vanishing, we get:

$$\begin{aligned} \mathbf{j}(\mathbf{r}_k) \simeq & \frac{e}{\mathcal{V}_{\text{cell}}\hbar}\sum_j(\mathbf{r}_j - \mathbf{r}_k)\int_{-\infty}^{E_F}dE\mathfrak{S}\{\tilde{t}_{kj}G_{jk}^<(E)\} \\ & + \frac{e^2}{\hbar}\sum_{q=1}^{N_L}V_q\sum_j\frac{\mathbf{r}_j - \mathbf{r}_k}{\mathcal{V}_{\text{cell}}}\mathfrak{S}\{\tilde{t}_{kj}\mathcal{C}_{jk}^q(E_F)\}, \end{aligned} \quad (7)$$

where we have defined the correlation functions due to the individual leads as $\mathcal{C}_{jk}^q = [G^r\Gamma_qG^a]_{jk}$. The first line in Eq. (7) represents the persistent current density (if any), while the second one describes the current induced by voltage drops (or equivalently currents) across the leads.

Note that in a tight-binding system with only nearest neighbor hoppings, the bonds contributing to the current density are only those connecting nearest neighbor sites. In our effective theory, the cavity vacuum fields mediate long-range hoppings \tilde{t}_{jk} , with j and k running throughout the whole sample.

III. MULTI-TERMINAL QUANTUM HALL BAR

As a first example to which we apply our theory, we will consider a multi-terminal quantum Hall bar, hosting a two-dimensional electron gas (2DEG) subjected to a

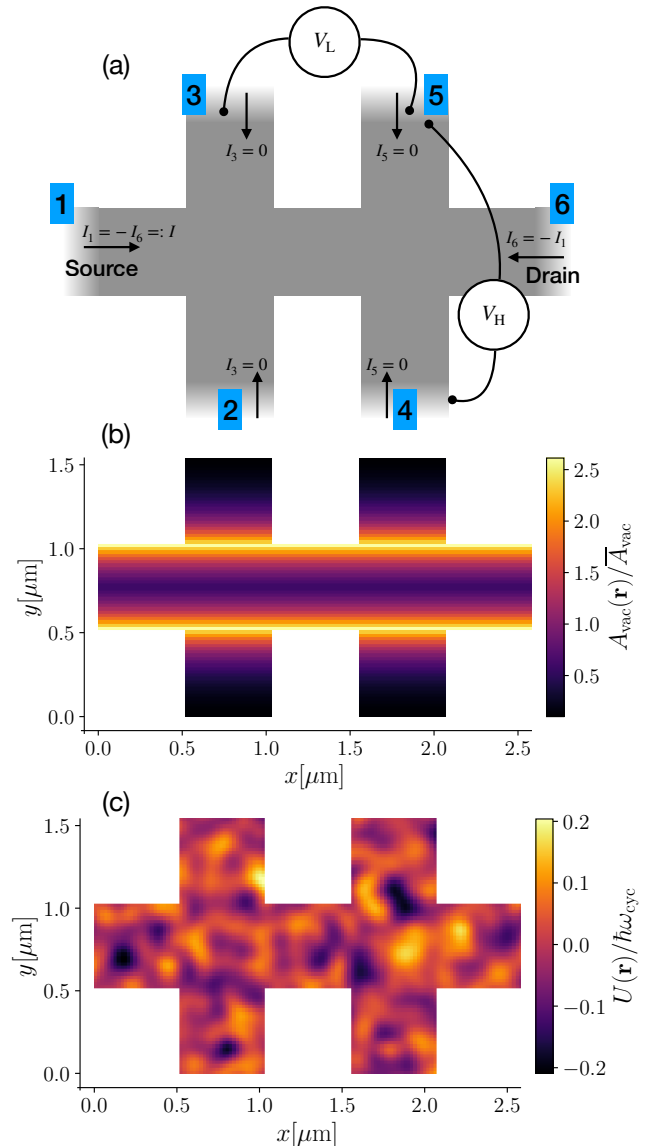


FIG. 1. (a): sketch of the six-terminal quantum Hall bar. (b): spatial dependence of the considered cavity mode vector potential. (c): disorder energy potential with a finite correlation length, $\lambda_{\text{corr}} = 60$ nm. In (a), the dark grey region corresponds to the scattering region, whereas the fading grey ones to the leads. In (b), The field strength is vertically proportional to an exponential decay: $A_{\text{vac}}(\mathbf{r}) \propto e^{-d(y)/\lambda}$, with $d(y)$ being the distance from the closest horizontal edge and $\lambda = 0.16 \mu\text{m}$, a characteristic length scale.

perpendicular magnetic field $\mathbf{B} = B\mathbf{e}_z$. The bare single-electron Hamiltonian is given by:

$$\hat{h} = \frac{1}{2m_*}[\hat{\mathbf{p}} - e\mathbf{A}_0(\hat{\mathbf{r}})]^2 + U(\hat{\mathbf{r}}), \quad (8)$$

where $\hat{\mathbf{p}} = \hat{p}_x\mathbf{e}_x + \hat{p}_y\mathbf{e}_y$ is the electron's momentum, m_* is its effective mass, and e is the electron charge. The operator $\hat{\mathbf{r}} = \hat{x}\mathbf{e}_x + \hat{y}\mathbf{e}_y$ represents the electron's position, while $U(\hat{\mathbf{r}})$ denotes a confining and/or disorder potential.

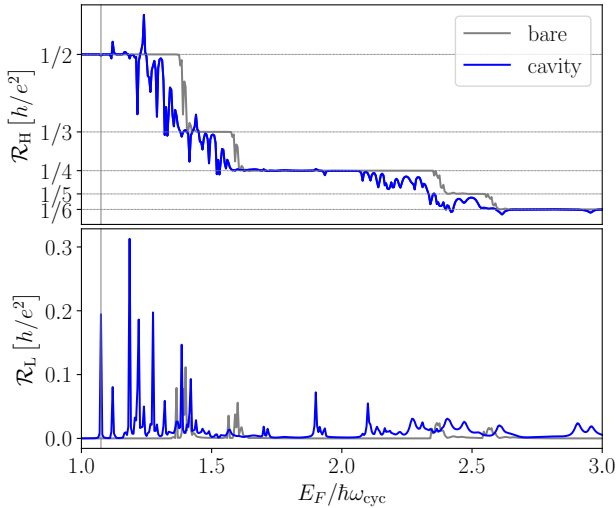


FIG. 2. Longitudinal (upper panel) and Hall resistances (lower panel) of a 2D Hall bar as a function of the Fermi level. The cavity-modified resistance is given in blue, while the bare one (no cavity coupling) in grey. The Hall bar is subject to a magnetic field $B = 0.1\text{T}$ and to an electronic disorder pictured in Fig. 1. Other parameters: discretization grid spacing $a = 10\text{ nm}$, $m_* = 0.067m_e$ (corresponding to GaAs), with m_e being the free electron mass, $E_Z = 0.2 \times \hbar\omega_{\text{cyc}}$. The cavity field is polarized along the x direction and its amplitude is given by $A_{\text{vac}}(\mathbf{r}) = A_{\text{vac}}(y) = \bar{A}_{\text{vac}} \times \mathcal{A}(y)$, with $\bar{A}_{\text{vac}} = \frac{\hbar\omega_{\text{cav}}}{2\pi c e} \sqrt{\alpha_{\text{fsc}}/\eta}$ being fixed by the compression factor $\eta = 10^{-10}$ and the cavity mode angular frequency $\omega_{\text{cav}} = 2\pi \times 10^{12}\text{rad/s}$. We include $\mathcal{A}(y)$, a modulation profile pictured in Fig. 1, to account for the spatial inhomogeneity of the field. We have introduced c the speed of light and $\alpha_{\text{fsc}} \approx 1/137$ the fine structure constant.

The static magnetic field $\mathbf{B} = \nabla \times \mathbf{A}_0$ can be expressed in terms of a classical vector potential $\mathbf{A}_0(\hat{\mathbf{r}})$. The presence of the magnetic field influences the electron dynamics by quantizing its kinetic energy into discrete, equally spaced energy levels known as Landau levels. These Landau levels are crucial in defining the quantum Hall effect and lead to the formation of chiral edge modes when the system is finite [49]. The energy spacing is directly proportional to the magnetic field B and is expressed as $E_{\text{cyc}} = \hbar\omega_{\text{cyc}} = \hbar eB/m_*$. In order to perform numerical simulations, we have discretized this Hamiltonian onto a two-dimensional square lattice of spacing a . The lattice sites are labeled by their positions $\mathbf{r}_i = (x_i, y_i)$, yielding the tight-binding Hamiltonian:

$$\hat{H} = \sum_i (4t + U_i) \hat{d}_i^\dagger \hat{d}_i - t \sum_{\langle i,j \rangle} e^{i\phi_{ij}} \hat{d}_i^\dagger \hat{d}_j, \quad (9)$$

where $t = \hbar^2/(2m_*a^2)$ is the hopping parameter, and ϕ_{ij} represents the classical Peierls phase due to the static magnetic field. In the Landau gauge, this phase factor is given by $\phi_{ij} = y_j a \ell_{\text{cyc}}^{-2} \delta_{y_i, y_j}$, with $\ell_{\text{cyc}} = \sqrt{\hbar/eB}$ being the magnetic length. The potential $U_i = U(\mathbf{r}_i)$ accounts for any disorder or confinement effects. The continuum limit is recovered by letting the lattice spac-

ing going to zero. In all the numerical simulations, we have carefully verified such convergence. Knowing the bare tight-binding Hamiltonian \hat{H} , we have calculated the cavity-mediated effective Hamiltonian \hat{H}_{eff} with the procedure described above.

In our study, we have considered a six-terminal configuration where the Hall bar is connected to six electrodes, with two of them serving as the source and drain. Fig. 1 illustrates the shape and dimensions of the sample used in our numerical simulations. We label the leads from 1 to 6, as in Fig. 1(a). We calculate the 5×5 reduced resistance matrix $(\mathcal{R}_{pq})_{p,q \in \{1, \dots, 5\}}$ of the Hall bar numerically, using the NEGF formalism at any given E_F . In quantum Hall experiments, the Hall and longitudinal resistances are obtained by driving a current through the source and drain and measuring voltage drops across zero-current contacts on the same side of the current flow (longitudinal voltage V_L) and opposite sides (Hall voltage V_H). We can read out these voltages from the elements of the reduced resistance matrix \mathcal{R} . The sign of the currents is defined as positive for incoming currents and negative for outgoing currents. The current entering the source (lead 1) is $I_1 = I > 0$. Since there is only one drain (lead 6), we must have $I_2 = I_3 = I_4 = I_5 = 0$ and the conservation of current imposes $I_1 = -I_6 = -I$. The Hall and longitudinal resistances are hence obtained as follows:

$$\mathcal{R}_H = \frac{V_H}{I} = \left[\frac{V_4 - V_5}{I_1} \right] = \mathcal{R}_{41} - \mathcal{R}_{51}, \quad (10)$$

$$\mathcal{R}_L = \frac{V_L}{I} = \left[\frac{V_3 - V_5}{I_1} \right] = \mathcal{R}_{31} - \mathcal{R}_{51}, \quad (11)$$

where we have used Eq. (3) to obtain the terminal voltages, for the given terminal currents I_i and resistance matrix \mathcal{R} .

Let us now include the spin degree of freedom. The Zeeman energy due to the magnetic field lifts the spin energy degeneracy. The single body Hamiltonian \hat{h} of the spinless electron given in Eq. (8) is promoted to a spinor Hamiltonian

$$\hat{h}_{\text{spinful}} = \begin{pmatrix} \hat{h}_\uparrow & 0 \\ 0 & \hat{h}_\downarrow \end{pmatrix}, \quad (12)$$

with $\hat{h}_\uparrow = \hat{h} - (\frac{1}{2}g_*\mu_B B) \hat{\mathbb{1}}$ and $\hat{h}_\downarrow = \hat{h} + (\frac{1}{2}g_*\mu_B B) \hat{\mathbb{1}}$. Here, g_* is the effective g -factor and μ_B the Bohr magneton. In the absence of spin-orbit interaction and magnetic impurities, the spin channels are independent and conductances are simply additive, namely $G_{\text{tot}} = G_\uparrow + G_\downarrow$. The conductance can be expressed in terms of the spinless conductance matrix as:

$$G^{\text{tot}}(E_F) = G \left(E_F + \frac{1}{2}E_Z \right) + G \left(E_F - \frac{1}{2}E_Z \right), \quad (13)$$

with $E_Z = g_*\mu_B B$ and G being the conductance of the spinless model. Since we have a quantum light-matter interaction conserving the electron spin, this relation also

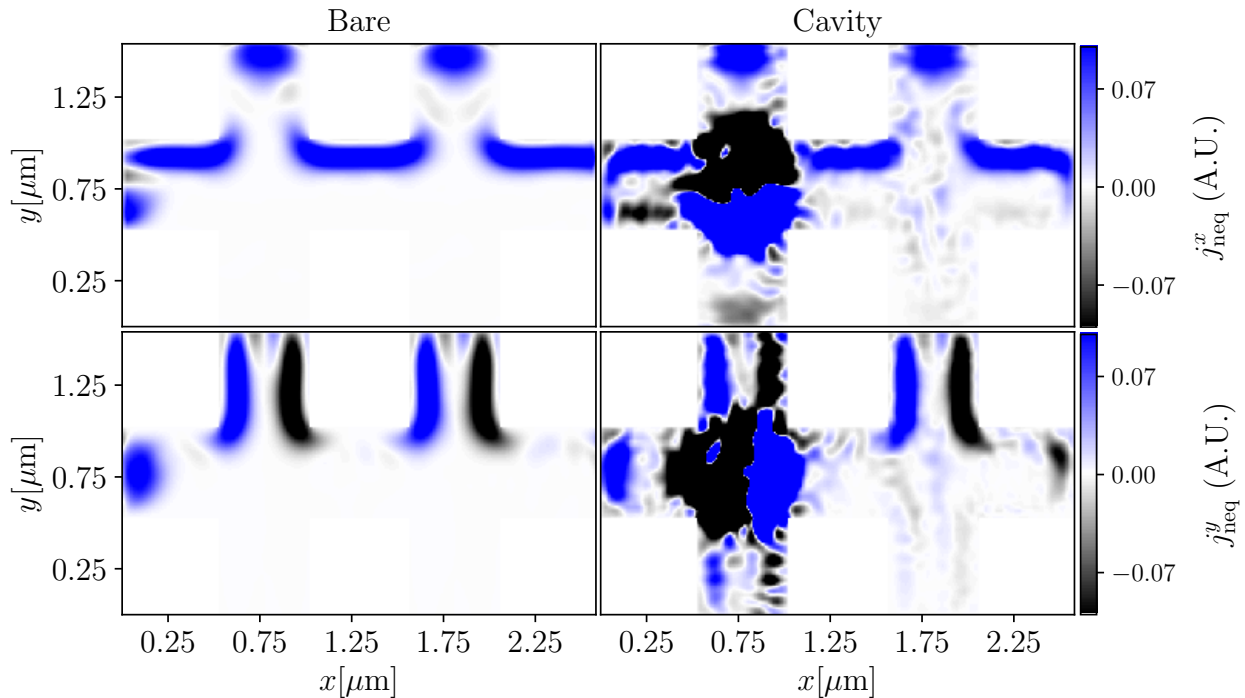


FIG. 3. Spatial-dependent current density profiles on the Hall bar, with same parameters as in Fig. 2. There is a net current imposed between leads 1 (source, left) and 6 (drain, right). The Fermi level is set to $E_F = 1.075 \times \hbar\omega_{\text{cyc}}$ (corresponding to the vertical line in the plots showing the magnetoresistances). The first column corresponds to the bare currents, while the second to the cavity-modified currents, showing inter-edge scattering. The first line represents the x -projection of the current density vector, while the second line, the y -projection.

holds for the cavity-modified conductance matrix. This conductance matrix is then used to compute the Hall and longitudinal resistances as usual. Following similar arguments, it can be shown that the following holds for the local currents and density of states

$$\mathbf{j}_{\text{neq}}^{\text{tot}}(\mathbf{r}_k; E_F) = \frac{e^2}{\hbar} \sum_{q=1}^{N_L} V_q \sum_j \frac{\mathbf{r}_j - \mathbf{r}_k}{a^2} \times \times \Im \left\{ \tilde{t}_{kj} \sum_{\sigma} G_{jk}^{n;q} \left(E_F + \sigma \frac{1}{2} E_Z \right) \right\}, \quad (14)$$

$$\rho^{\text{tot}}(\mathbf{r}_k; E_F) = \rho \left(\mathbf{r}_k; E_F + \frac{1}{2} E_Z \right) + \rho \left(\mathbf{r}_k; E_F - \frac{1}{2} E_Z \right). \quad (15)$$

To compute the local current density in the six-terminal device, we use the resistance matrix \mathcal{R} to express the voltages, leaving only the imposed current I as a free parameter. We replace the values of V_q as follows: we can set $\mu_6 = \sum_{0 \leq q < 5} \mu_q / 5 = E_F$, to have $V_6 = 0$ in turn as discussed earlier. By imposing our usual terminal

currents and using the current voltage relation, we get:

$$\mathbf{j}_{\text{neq}}(\mathbf{r}_k) = \frac{I}{a} \sum_j \left(\frac{\mathbf{r}_j - \mathbf{r}_k}{a} \right) \times \times \left[\sum_{q=1}^5 \left(\frac{e^2}{\hbar} \mathcal{R}_{q1} \right) \sum_{\sigma} \Im \left\{ t_{kj} G_{jk}^{n;q} \left(E_F + \frac{\sigma}{2} E_Z \right) \right\} \right]. \quad (16)$$

The resistance matrix elements \mathcal{R}_{q1} are computed by inverting the two-spin channel conduction matrix.

We have computed the Hall and longitudinal resistances for a range of Fermi levels and have reported our results in Fig. 2. Electronic disorder has been included in our sample, as shown in Fig. 1(c). This potential is generated as a random function with a finite correlation length. The cavity mode we consider has a spatially varying profile, depicted in Fig. 1(b). We have attempted to mimic the strong gradients along the Hall bar edges, reported in [40]. For more details on the cavity parameters refer to the caption in Fig. 2. We emphasize that with our theoretical framework we can consider electronic disordered potentials and cavity mode profiles of arbitrary shape, so what considered is just an illustrative and representative example.

The bare (no-cavity) Hall resistance shows distinct steps at quantized values $\mathcal{R}_H = h/(\nu e^2)$, where ν represents the number of fully filled Landau levels (includ-

ing spin). To be precise, $\nu(E_F) = \sum_{n\sigma} \mathbf{1}_{E_{n\sigma} < E_F}$, where $E_{n\sigma} = E_{\text{cyc}}(n + 1/2) + \sigma E_Z/2$, $n \in \mathbb{N}$ and $\sigma \in \{+1, -1\}$. The longitudinal resistance \mathcal{R}_L vanishes whenever E_F lies between two consecutive $E_{n\sigma}$ values and exhibits peaks when \mathcal{R}_H steps into a new plateau. These transition Fermi energies are $E_F \in \{E_{n\sigma}\}_{n\sigma}$. This magnetoresistance phenomenology is typical of the well-known integer quantum Hall effect. It occurs because the electrons flow along chiral edge modes without dissipation, while the bulk acts as an insulator. The only way to disrupt this effect is by enabling electrons to scatter ‘backwards’ [50], which means traveling to the edge that flows in the opposite direction. This process is called backscattering and is absent in the quantum Hall regime due to the insulating bulk. The edge states are said to be topologically protected. It can happen in narrow quantum Hall bars, but if the width is large enough inter-edge scattering becomes negligible.

In sharp contrast, for the considered Hall bar width, the cavity Hall resistance quantization breaks down and correspondingly a finite longitudinal resistance emerges at integer filling factors. The odd numbered plateaus (those for which ν is odd) are more sensitive to the cavity-induced long-range hopping if the Zeeman energy splitting is smaller than the cyclotron energy. This is because, since $E_Z \ll \hbar\omega_{\text{cyc}}$, at odd integer filling the plateaus are closer in energy. These findings are in agreement with experimental evidence in [36]. In Fig. 3, we show the non-equilibrium current density when current flows from terminal 1 to 6 at $E_F = 1.075 \times E_{\text{cyc}}$. The bare currents flow exclusively along the edge without any resistance. If we look at the x -projection of the currents, they are all in blue, meaning positive, flowing from left to right. In presence of the cavity, there are currents flowing backwards, carrying charge to the opposite edge and thus increasing resistance to the imposed current that flows from left to right. This is a result of cavity-mediated inter-edge scattering [16].

To conclude this section, we would like to make a few remarks about the computational complexity of our cavity-modified quantum transport calculations. The continuum limit of the discretized model is obtained when $E_F \ll 2t = \hbar^2/(m_*a^2)$, with a being the lattice spacing. Here we have scanned E_F over a range $\{\nu\hbar\omega_{\text{cyc}}; \nu \in [1, 3]\}$. The continuum limit condition for ν is hence given by $\nu \ll (\ell_{\text{cyc}}/a)^2$. For a lead width $l_W = 0.5 \mu\text{m}$, we can express the continuum limit condition again as $\nu \ll 0.0025 \times (N_W^2/B[\text{T}])^2$, with N_W being the number of discretisation points along the lead’s width and $B[\text{T}]$ being the magnetic field in units of Tesla. The reported simulations have been carried out for $N_W = 25$ and $B = 0.1 \text{T}$. In order to simulate a field 16 times stronger, namely $B = 1.6 \text{T}$, at the same convergence to the continuum limit rate, we would need a grid 4 times finer [51].

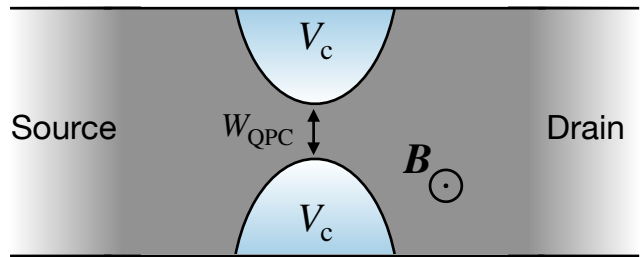


FIG. 4. Sketch of a Quantum Point Contact (QPC). The cyan blobs are regions with a constant and high constriction potential barrier $V_c \gg \hbar\omega_{\text{cyc}}$. The distance between the boundaries of these regions is W_{QPC} . In the following calculations, we have considered a barrier region defined by the boundary $f_{\text{bound}}(\tilde{x}) = \frac{L_y - W_{\text{QPC}}}{2} \exp\left[-\frac{(\tilde{x}/\delta)^2}{1 - (\tilde{x}/\delta)^2}\right]$ for $-\delta \leq \tilde{x} \leq \delta$ and $f_{\text{bound}}(\tilde{x}) = 0$ otherwise. In all the reported calculations, we have taken $\delta = 20 \text{ nm}$. The horizontal coordinate \tilde{x} is zero in the middle of the barrier region.

IV. QUANTUM POINT CONTACTS

A quantum point contact (QPC) is a narrow constriction between two wider electron gas regions, often fabricated on a 2DEG system [52]. We shall study the case when the 2DEG is coupled to a strong perpendicular magnetic field. Given the chiral nature of edge states in quantum Hall physics, bringing the edges close together generates interesting effects, as the states on opposing sides propagate in opposite directions. We consider a 2DEG confined to a rectangular slab under a strong perpendicular magnetic field. The Hamiltonian governing this system is the one used for the six-terminal Hall bar (see Eq. (9)), but the geometry here is simpler, consisting of a rectangular $L_x \times L_y$ slab connected to only two leads along the x -axis. To impose a constriction in the transverse direction, we consider a strong and constant potential barrier, as shown in Fig. 4. In the following, we will simplify our analysis by considering only one spin channel. We are interested in investigating how the width of the constriction, W_{QPC} , and cavity vacuum fields influence the two-terminal conductance, the local density of states, and the local current densities.

In Fig. 5, first plot from the left, we present the conductance curve as a function of Fermi energy for three different values of W_{QPC} , with thicker lines representing larger openings. The first notable feature is the quantization of conductance, which is characteristic of quantum Hall systems. This conductance quantization persists in QPCs even without the need of a magnetic field. As expected from numerous experimental and theoretical works, reducing W_{QPC} brings the edges closer and introduces backscattering leading to an increased resistance. We see that conductance is toned down as the width becomes smaller. This phenomenon is more prominent at higher filling, since the edge states penetrate more in the bulk. Bringing together two edge states from opposite sides allows electrons to flow in the opposite direction of

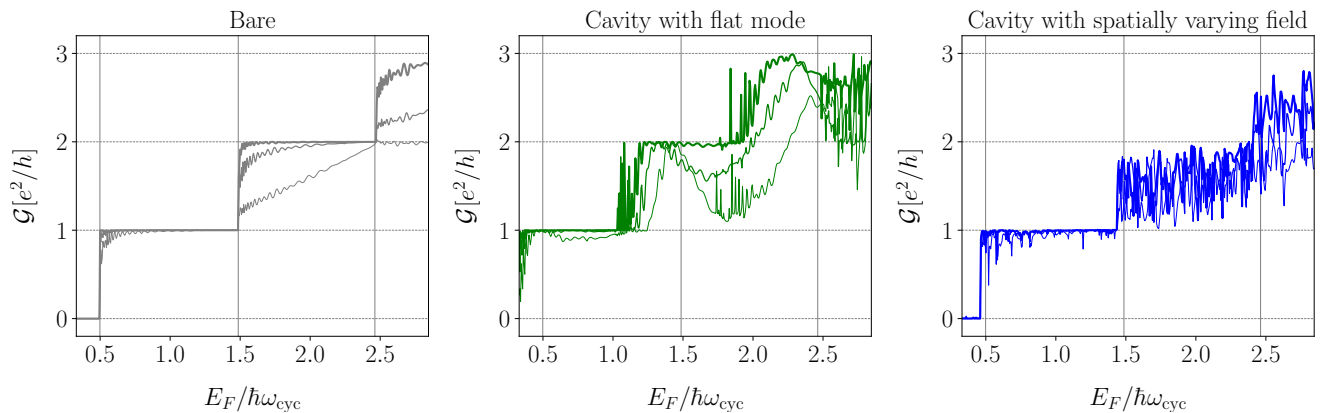


FIG. 5. Two-terminal conductance (only a single spin channel is considered) of a quantum point contact with varying constriction widths as a function of Fermi energy. From left to right, the first plot shows the bare conductance (no cavity coupling), the second shows conductance for a sample with flat cavity mode (no spatial gradients) and the third one for a spatially-varying mode. Parameters of calculations: rectangular slab with dimensions $L_x \times L_y = 600 \text{ nm} \times 150 \text{ nm}$, $m_* = 0.067 \times m_e$, $B = 6 \text{ T}$, $a = 2 \text{ nm}$, $V_c = 100 \times \hbar\omega_{\text{cyc}}$. The distance between the lower and upper regions, W_{QPC} , has been set to different values: 32 nm, 40 nm and 48 nm and in the plots, the linewidths are proportional to the constriction width. Other parameters: $\omega_{\text{cav}} = 2\pi \times 10^{12} \text{ rad/s}$ and $\eta = 3 \times 10^{-11}$ (see caption of Fig. 2 for details on how the amplitude of the vector potential is defined). The polarisation vector is along the y direction. For the third plot, the mode profile is x -dependent: $A(x) = 0.5$ for $0 \leq x[\text{nm}] \leq 225$, $= 1.5$ for $375 \leq x[\text{nm}] \leq 600$, and increasing linearly from $x = 225 \text{ nm}$ to $x = 325 \text{ nm}$.

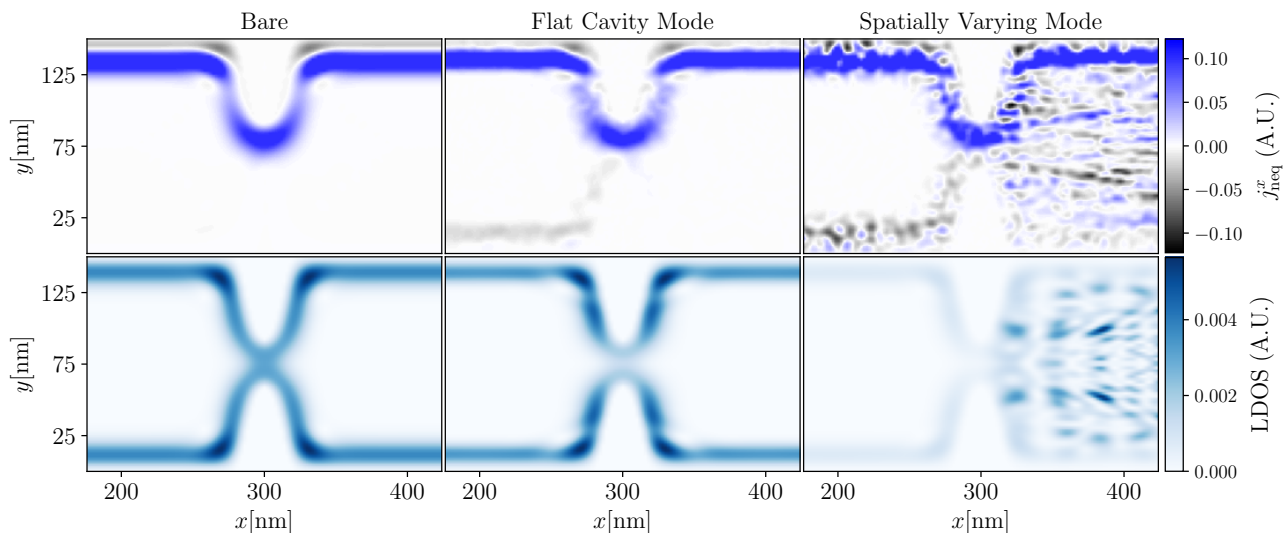


FIG. 6. Non-equilibrium current density and local densities of states for Hall bar quantum point contacts of width $W_{\text{QPC}} = 32 \text{ nm}$ at filling $E_F = 0.825 \times \hbar\omega_{\text{cyc}}$ with no cavity, flat mode and a gradient field. We have imposed a potential difference $V_L > V_R$, so that current flows from left to right. The electronic system and the cavity parameters are the same as the one described in Fig. 5. The first row of panels shows the x -projection of the current density $\mathbf{j}_{\text{neq}} \cdot \mathbf{e}_x$. The second row of panels shows the local density of states. Only the central region, close to the constriction is showed here.

the imposed voltage gradient. This phenomenon disrupts the system's topology.

In the second and third plots of Fig. 5, we present the conductance curves modified by the cavity. While there is a slight shift in energy levels, the most notable feature is the near-complete destruction of quantized plateaus. The second plot corresponds to a flat cavity mode, while the third reflects a cavity mode with a gradient at the contact. Further details are provided in the caption of Fig. 5. Despite the destruction of quantization, the conduc-

tance still exhibits the characteristic of increasing with larger openings. The spatially varying cavity mode appears to have a stronger impact on the system, due to a stronger breaking of translational invariance. This results in significant deviations from quantization, caused by cavity-mediated hopping [16].

In the first row of Fig. 6, we plot the x -component of the non-equilibrium currents at a fixed Fermi level $E_F = 0.825 \times E_{\text{cyc}}$, just above the first Landau level (where only one edge state is present), and a fixed quan-

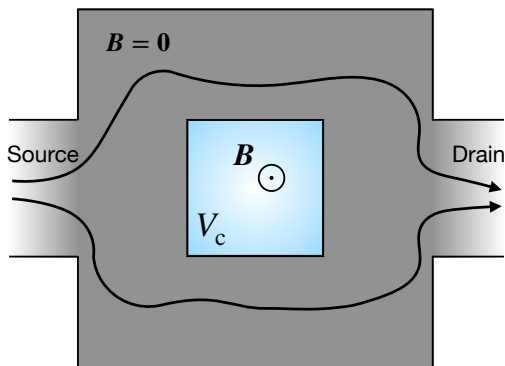


FIG. 7. Sketch of the Aharonov Bohm interferometer. The cyan square in the middle is pierced by a magnetic field \mathbf{B} . We have imposed a very large constriction potential V_c potential on that part to prevent electrons from flowing on the region with magnetic field. The two arrows represent two paths the electron could take in going from left to right. The source and drain here serve also as contacts.

tum point contact (QPC) opening $W_{\text{QPC}} = 32\text{nm}$ for the three cases: bare, flat cavity mode, and spatially varying cavity mode. It is clear that cavity coupling creates backscattering along the lower edge through cavity-mediated electron hopping. Moreover, it leads to the formation of new bulk states in the case of a spatially varying cavity mode as witnessed by the new peaks in the local density of states.

V. AHARONOV-BOHM INTERFEROMETERS

The last type of device we consider in this article are electron interferometers based on the celebrated Aharonov-Bohm (AB) effect, which is remarkable as it shows that charged particles are influenced by electromagnetic potentials, even in regions where the magnetic and electric fields are strictly zero [53]. An AB interferometer can be achieved by splitting an electron beam and directing it around a region with a confined magnetic field, such as inside a solenoid. Despite the electrons never entering the magnetic field, they experience a phase shift due to the non-zero vector potential. This phase shift leads to observable interference patterns, such as conductance through an AB interferometer, which we shall study here.

The AB interferometer we consider consists of a 2D system with a hole in the middle, through which there is a magnetic flux going through. The region where electrons can travel has zero magnetic field. In Fig. 7 we have drawn a sketch of our device. The phase picked by the electronic wavefunction around the hole is proportional to the applied magnetic flux. For a given Fermi Energy E_F the conductance is a periodic function of the applied magnetic flux, namely $\mathcal{G}(E_F, \Phi + n\Phi_0) = \mathcal{G}(E_F, \Phi)$ for every integer n and where $\Phi_0 = h/e$ is the flux quantum. Note also that, due to the Onsager-Büttiker relation [54],

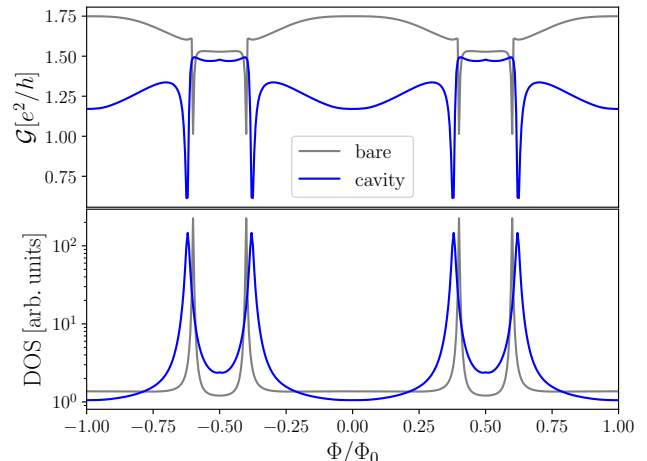


FIG. 8. Conductance (upper panel) and density of states (lower panel) as a function of magnetic flux over two periods. The grey curve is for the bare case, while blue refers to the cavity case. The Fermi energy is $E_F = 10\text{meV}$. The sample has dimensions $L_x \times L_y = 150\text{nm} \times 150\text{nm}$, with the square hole in the middle having a side length of $l = 50\text{nm}$. The leads are connected to the left and right sides of the sample and their width is a third of the sample's side length, i.e. 50nm . There is no electronic disorder in the calculation and the cavity is polarised along the transverse direction with $\omega_{\text{cav}} = 2\pi \times 10^{12}\text{rad/s}$ and $\eta = 3 \times 10^{-11}$. The wall potential is $V_c = 10\text{eV} \gg E_F$, ensuring the electrons to remain outside of the $B \neq 0$ area. Other parameters: $m_* = 0.067m_e$, $a = 2\text{nm}$.

for any two-terminal device the conductance is an even function of the magnetic flux $\mathcal{G}(E_F, \Phi) = \mathcal{G}(E_F, -\Phi)$. Note that such properties remain unchanged in presence of the cavity coupling. As an illustrative example, we have presented in Fig. 8 the variation of the conductance with respect to the applied magnetic flux, showing that such conductance is an even function of Φ and with period equal to Φ_0 .

In Fig. 9, we report the current density for two different fluxes (left and right columns) for the case without the cavity (top row) and with the cavity (bottom row). This figure simply illustrates the sensitivity of the current patterns to the applied flux bias and how the cavity vacuum fields can non-trivially modify such pattern and hence the interference measured in the two-terminal conductance.

A key figure of merit of an AB devices is the interference visibility, which can be defined as:

$$\Lambda(E_F) = \frac{\max_{\Phi} \mathcal{G}(E_F; \Phi) - \min_{\Phi} \mathcal{G}(E_F; \Phi)}{\max_{\Phi} \mathcal{G}(E_F; \Phi)}. \quad (17)$$

In Fig. 10, we have shown the visibility curve $\Lambda(E_F)$ in a relatively wide range of Fermi energies for the bare device (grey line) and in presence of the cavity coupling (blue). The irregular shape of the visibility is due to the complex density of states in the considered device geometry. This

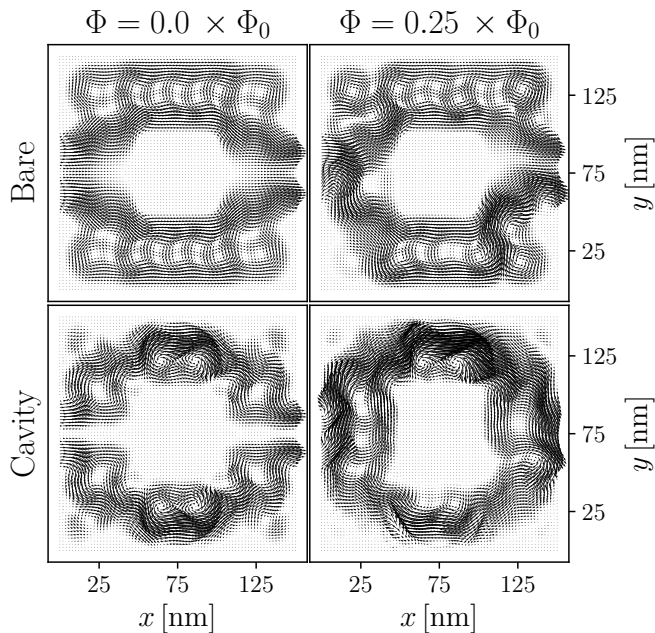


FIG. 9. Vector field plot for the non-equilibrium current density $\mathbf{j}_{\text{neq}}(\mathbf{r})$ in the considered Aharonov-Bohm interferometer. The Fermi energy is set to $E_F = 12.9$ meV. The flux is set to the values reported on top of each column. Other parameters are as in Fig. 8.

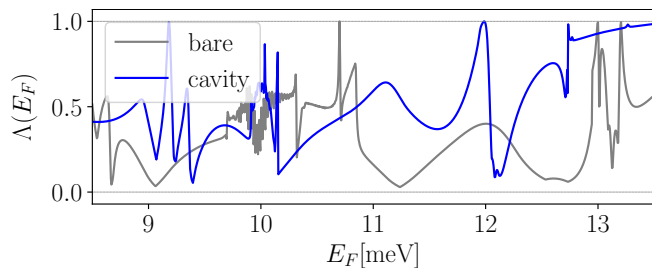


FIG. 10. The visibility $\Lambda(E_F)$ of the considered Aharonov-Bohm interferometer. For each E_F , the conductance has been sampled for 200 different equally-spaced values of $\Phi \in [0, \Phi_0]$. Other parameters are as in Fig. 8.

is illustrated in Fig. 11, which shows the conductance of the device in the same range of Fermi energies and the corresponding density of states. The influence of the cavity vacuum fields is both dramatic on the shape of the interference visibility, the conductance and the density of states.

Note that density of states and conductance are correlated for both the bare and the cavity case. A peak in the DOS curve corresponds to a kink in conductance. From the DOS curve, we see that the cavity is able to alter the spectral properties of the material dictating new transport properties. The very irregular structure of the curves we have reported here, comes as a consequence of the shape of the device. In absence of magnetic field, the bulk conducts. The said modes have irregular profiles due to the complicated shape of the boundary conditions.

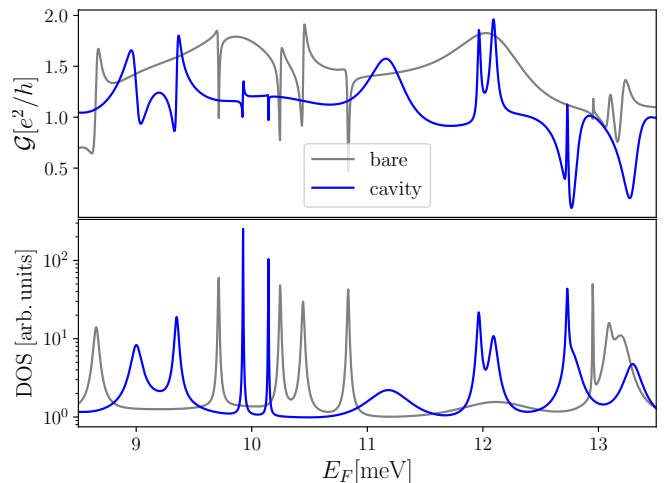


FIG. 11. Conductance (upper panel) and density of states (lower panel) of the considered Aharonov Bohm interferometer as a function of Fermi energy. The flux is fixed at $\Phi = 0.11 \times \Phi_0$. Other parameters are as in Fig. 8.

Semi-classically, electrons can go in straight lines, bouncing and reflecting on the boundaries of the sample. This billiard ball scheme couples many interference patterns. We note that the cavity alters this structure by creating new paths for electrons to travel.

VI. CONCLUSIONS AND OUTLOOK

In this work, we have explored the role of cavity-mediated electron hopping in influencing a variety of quantum transport devices, including multi-terminal quantum Hall bars, quantum point contacts, and Aharonov-Bohm electronic interferometers. Specifically, we have investigated the impact of cavity vacuum fields not only on macroscopic observables such as conductance and resistance but also on microscopic properties like current patterns and the local density of states. Notably, we have uncovered a rich phenomenology of cavity-mediated inter-edge scattering in narrow quantum Hall bars and quantum point contacts. Additionally, we have demonstrated that strong vacuum fields can qualitatively affect the interference visibility in Aharonov-Bohm devices. Our findings emphasize that strong vacuum fields—whether intentionally introduced or unintentionally generated by metallic contacts and gates acting as antennas—must be carefully considered in the design and analysis of mesoscopic quantum devices.

Looking forward, the formalism and methodologies developed in this study offer promising avenues for further exploration. One such direction is the application of this cavity-modified quantum transport framework to materials such as graphene and other tight-binding systems. Graphene, with its unique electronic properties—including a linear dispersion relation and topological features—presents an ideal platform for probing new

regimes of quantum transport under the influence of cavity fields. Similarly, this approach can be extended to other low-dimensional materials, such as transition metal dichalcogenides (TMDs) and engineered lattices, where light-matter interactions may enable novel means of controlling electronic properties.

Moreover, a critical direction for future work is extending this framework to regimes where cavity vacuum fields cannot be adiabatically eliminated and light-matter entanglement becomes a dominant factor. These regimes, where the quantum nature of the cavity field is inseparable from the electronic degrees of freedom, could reveal fundamentally new quantum transport phenomena. Understanding such entangled light-matter systems will be key to harnessing quantum correlations and exploring the interplay between photonic and electronic excitations.

Future investigations could also broaden the scope of this formalism to include interactions between cavity fields and superconducting systems, fractional quantum Hall states, and even non-equilibrium dynamics in driven systems. These efforts have the potential to uncover new quantum transport phenomena and pave the way for the development of innovative quantum devices that exploit cavity-induced effects.

ACKNOWLEDGMENTS

We acknowledge financial support from the French agency ANR through the project CaVdW (ANR-21-CE30-0056-0) and from the Israeli Council for Higher Education - VATAT.

Appendix A: Self-energy of the leads in a 2DEG

In this Appendix, we report details about the determination of the self-energies due to the contact leads. Let us consider first a finite-size 2D system coupled to a single lead. In particular, the system is assumed to have a finite size in the transverse y direction and to be semi-infinite in the longitudinal x direction. The Hamiltonian of the such bipartite system reads:

$$\begin{pmatrix} \hat{h} & \hat{\tau} \\ \hat{\tau}^\dagger & \hat{H} \end{pmatrix}, \quad (\text{A1})$$

where \hat{h} is the Hamiltonian of the lead, \hat{H} is the Hamiltonian of the device system and $\hat{\tau}$ is the coupling matrix of the system to the leads. The contact Hamiltonian is

$$\hat{h} = 4t \sum_{\iota} |\iota\rangle\langle\iota| - t \sum_{\langle\iota,\kappa\rangle} |\iota\rangle\langle\kappa|, \quad (\text{A2})$$

where the boundary conditions are implicit. The system-lead coupling is only along the interface, namely

$$\langle\iota|\hat{\tau}_q|i\rangle = \begin{cases} -t & \text{if } |\mathbf{r}_\iota - \mathbf{r}_i| = a \\ 0 & \text{otherwise} \end{cases}, \quad (\text{A3})$$

where ι is a site of the lead and i is a site of the system. The corresponding retarded self-energy for the system due to the lead is given by $\hat{\Sigma}^r = \hat{\tau}^\dagger \hat{g}^r \hat{\tau}$. This means that $\langle i|\Sigma^r|j\rangle = 0$ if either i or j is not along the system-lead interface and $\langle i|\Sigma^r|j\rangle = t^2 \langle\iota|g^r|\kappa\rangle$, where here ι (resp. κ) is the nearest neighbor site in the lead of the system site i (resp. j). This implies that we only need to compute g^r along the interface with the conductor.

The lead Green's function is obtained by first inverting the $(E - \hat{h} + i\eta)$ matrix for a finite-size lead and then letting the number of sites N_x along its longitudinal dimension to infinity, keeping the transverse one fixed. Note that it is essential to keep $\eta > 0$ and letting it tend to 0^+ only after taking the $N_x \rightarrow +\infty$ limit. Each site on the lead is denoted by an index ι , positioned at $\mathbf{r}_\iota = (x_\iota, y_\iota)$. It is convenient to represent \hat{h} in terms of its eigenstates $|\chi_{\alpha,\beta}\rangle$ defined by the eigenvalue equation $\hat{h}|\chi_{\alpha,\beta}\rangle = (\varepsilon_\alpha^x + \varepsilon_\beta^y)|\chi_{\alpha,\beta}\rangle$, with

$$\langle\iota|\chi_{\alpha,\beta}\rangle = \chi_\alpha^x(x_\iota)\chi_\beta^y(y_\iota), \quad (\text{A4})$$

$$\chi_\alpha^x(x_\iota) = \sqrt{\frac{2}{N_x+1}} \sin\left(\alpha \frac{\pi}{N_x+1} \frac{x_\iota}{a}\right), \quad (\text{A5})$$

$$\varepsilon_\alpha^x = 2t \left[1 - \cos\left(\alpha \frac{\pi}{N_x+1}\right) \right], \quad (\text{A6})$$

$$\chi_\beta^y(y_\iota) = \sqrt{\frac{2}{N_y+1}} \sin\left(\beta \frac{\pi}{N_y+1} \frac{y_\iota}{a}\right), \quad (\text{A7})$$

$$\varepsilon_\beta^y = 2t \left[1 - \cos\left(\beta \frac{\pi}{N_y+1}\right) \right]. \quad (\text{A8})$$

Note that here $\alpha \in \{1, \dots, N_x\}$ and $\beta \in \{1, \dots, N_y\}$ correspond to the longitudinal and transverse direction respectively. Using the spectral representation, we obtain the Green's function for the isolated lead on the surface, i.e. for the sites closest to the system (\mathbf{r}_ι such that $x_\iota = a$, supposing without loss of generality that the system is situated at $x \leq 0$). Hence, we find

$$\langle\iota|\hat{g}^r(E)|\kappa\rangle = \sum_{\mu=1}^{N_y} \chi_\mu^y(y_\iota)\chi_\mu^y(y_\kappa)^* \sum_{\nu=1}^{N_x} \frac{\chi_\nu^x(a)\chi_\nu^x(a)^*}{E - \varepsilon_\mu^y - \varepsilon_\nu^x + i\eta}. \quad (\text{A9})$$

From this, we can evaluate the Green's function of the infinite system in the limit $N_x \rightarrow +\infty$ by recognizing a Riemann sum

$$\begin{aligned} \langle\iota|g^r(E)|\kappa\rangle &= -\frac{1}{t} \sum_{\mu=1}^{N_y} \chi_\mu^y(y_\iota)\chi_\mu^y(y_\kappa)^* \times \\ &\times \lim_{N_x \rightarrow \infty} \sum_{\nu=1}^{N_x} \left(\frac{\pi}{N_x+1}\right) f_{\mu,E} \left(\nu \frac{\pi}{N_x+1}\right) \\ &= -\frac{1}{t} \sum_{\mu=1}^{N_y} \chi_\mu^y(y_\iota)\chi_\mu^y(y_\kappa)^* \int_0^\pi dx f_{\mu,E}(x), \end{aligned} \quad (\text{A10})$$

where we have defined:

$$f_{\mu,E}(x) = \frac{2}{\pi} \frac{-\sin^2 x}{\tilde{E}_{y\mu} + i\eta + 2 \cos x} \quad (\text{A11})$$

and $\tilde{E}_{y\mu} = \frac{1}{t}(E - 2t - \varepsilon_\mu^y)$. By extending the integral over a full period and changing variables, it can be expressed

$$\frac{1}{2i\pi} \oint_{\mathbb{S}^1} dz \frac{z^2 - 1}{1 + (\tilde{E}_{y\mu} + i\eta)z + z^2} = \begin{cases} \frac{1}{2} \left(-\tilde{E}_{y\mu} + \text{sgn}(\tilde{E}_{y\mu}) \sqrt{\tilde{E}_{y\mu}^2 - 4} \right), & \text{for } |\tilde{E}_{y\mu}| > 2 \\ \frac{1}{2} \left(-\tilde{E}_{y\mu} + i\sqrt{4 - \tilde{E}_{y\mu}^2} \right), & \text{for } |\tilde{E}_{y\mu}| \leq 2 \end{cases}. \quad (\text{A13})$$

There is one crucial point we would like to point out. In case there is a lead connected to the scattering device subjected to a gauge field that picks the phase along the direction parallel to the transverse modes in the lead, we should make sure that the wavefunctions $\chi_\mu^y(y_j)$ account for that. Since there is no B field in the leads, we must assure a constant gauge along the leads, that

as a contour integral over the unit circle:

$$\int_0^\pi dx f_{\mu,E}(x) = \frac{1}{2i\pi} \oint_{\mathbb{S}^1} dz \frac{z^2 - 1}{1 + (\tilde{E}_{y\mu} + i\eta)z + z^2}, \quad (\text{A12})$$

with $\eta \rightarrow 0^+$ in the end. The result obtained using the residue theorem is the following:

extends by continuity from the device. This is handled by adding on the transverse modes the same phase as the one picked along the boundary of the device. The expression of $\chi_\mu^y(y_j)$ is modified. However, we obtain it numerically, by solving the 1D tight-binding particle on a finite chain, with a gauge where a constant phase, equal to that on the boundary of the device, is picked along the chain.

-
- [1] F. J. Garcia-Vidal, C. Ciuti, and T. W. Ebbesen, Manipulating matter by strong coupling to vacuum fields, *Science* **373** (2021).
- [2] F. Schlawin, D. M. Kennes, and M. A. Sentef, Cavity quantum materials, *Applied Physics Reviews* **9**, 011312 (2022).
- [3] J. Bloch, A. Cavalleri, V. Galitski, M. Hafezi, and A. Rubio, Strongly correlated electron–photon systems, *Nature* **606**, 41 (2022), perspective, Published: 25 May 2022.
- [4] G. Scalari, C. Maissen, D. Turčinková, D. Hagenmüller, S. De Liberato, C. Ciuti, C. Reichl, D. Schuh, W. Wegscheider, M. Beck, *et al.*, Ultrastrong coupling of the cyclotron transition of a 2d electron gas to a 2d metamaterial, *Science* **335**, 1323 (2012).
- [5] J. Keller, G. Scalari, S. Cibella, C. Maissen, F. Apugliese, E. Giovine, R. Leoni, M. Beck, and J. Faist, Few-electron ultrastrong light-matter coupling at 300 GHz with nanogap hybrid LC microcavities, *Nano Letters* **17**, 7410 (2017).
- [6] Y. Ashida, A. İmamoğlu, and E. Demler, Cavity Quantum Electrodynamics with hyperbolic van der Waals materials, *Physical Review Letters* **130**, 216901 (2023).
- [7] H. Herzig Sheinfux, L. Orsini, M. Jung, I. Torre, M. Cecanti, S. Marconi, R. Maniyara, D. Barcons Ruiz, A. Hötger, R. Bertini, *et al.*, High-quality nanocavities through multimodal confinement of hyperbolic polaritons in hexagonal boron nitride, *Nature Materials* **23**, 499 (2024).
- [8] P. Forn-Díaz, L. Lamata, E. Rico, J. Kono, and E. Solano, Ultrastrong coupling regimes of light-matter interaction, *Reviews of Modern Physics* **91** (2019).
- [9] A. F. Kockum, A. Miranowicz, S. D. Liberato, S. Savasta, and F. Nori, Ultrastrong coupling between light and matter, *Nature Reviews Physics* **1**, 19 (2019).
- [10] F. Schlawin, A. Cavalleri, and D. Jaksch, Cavity-mediated electron-photon superconductivity, *Physical review letters* **122**, 133602 (2019).
- [11] J. B. Curtis, Z. M. Raines, A. A. Allocca, M. Hafezi, and V. M. Galitski, Cavity Quantum Eliashberg Enhancement of Superconductivity, *Physical Review Letters* **122** (2019).
- [12] M. A. Sentef, M. Ruggenthaler, and A. Rubio, Cavity Quantum-Electrodynamical polaritonically enhanced electron-phonon coupling and its influence on superconductivity, *Science advances* **4**, eaau6969 (2018).
- [13] O. Dmytruk and M. Schirò, Controlling topological phases of matter with quantum light, *Communications Physics* **5** (2022).
- [14] V. K. Kozin, E. Thingstad, D. Loss, and J. Klinovaja, Cavity-enhanced superconductivity via band engineering, *arXiv preprint arXiv:2405.08642* (2024).
- [15] F. Méndez-Córdoba, J. Mendoza-Arenas, F. Gómez-Ruiz, F. Rodríguez, C. Tejedor, and L. Quiroga, Rényi entropy singularities as signatures of topological criticality in coupled photon-fermion systems, *Physical Review Research* **2**, 043264 (2020).
- [16] C. Ciuti, Cavity-mediated electron hopping in disordered quantum Hall systems, *Physical Review B* **104** (2021).
- [17] D.-P. Nguyen, G. Arwas, Z. Lin, W. Yao, and C. Ciuti, Electron-Photon Chern Number in Cavity-Embedded 2D Moiré Materials, *Physical Review Letters* **131** (2023).
- [18] B. Pérez-González, G. Platero, and Á. Gómez-León,

- Light-matter correlations in quantum Floquet engineering, [arXiv preprint arXiv:2302.12290](#) (2023).
- [19] Z. Lin, C. Xiao, D.-P. Nguyen, G. Arwas, C. Ciuti, and W. Yao, Remote gate control of topological transitions in moiré superlattices via cavity vacuum fields, *Proceedings of the National Academy of Sciences* **120** (2023).
- [20] F. Méndez-Córdoba, F. Rodríguez, C. Tejedor, and L. Quiroga, From edge to bulk: Cavity-induced displacement of topological nonlocal qubits, *Physical Review B* **107**, 125104 (2023).
- [21] D.-P. Nguyen, G. Arwas, and C. Ciuti, Electron conductance and many-body marker of a cavity-embedded topological one-dimensional chain, *Phys. Rev. B* **110**, 195416 (2024).
- [22] O. Dmytruk and M. Schirò, Hybrid light-matter states in topological superconductors coupled to cavity photons, *Physical Review B* **110**, 075416 (2024).
- [23] Á. Gómez-León, M. Schirò, and O. Dmytruk, High-quality poor man’s majorana bound states from cavity embedding, [arXiv preprint arXiv:2407.12088](#) (2024).
- [24] D. Shaffer, M. Claassen, A. Srivastava, and L. H. Santos, Entanglement and topology in Su-Schrieffer-Heeger cavity quantum electrodynamics, *Physical Review B* **109**, 155160 (2024).
- [25] Z. Bacciconi, G. M. Andolina, and C. Mora, Topological protection of majorana polaritons in a cavity, *Physical Review B* **109**, 165434 (2024).
- [26] L. Yang and Q.-D. Jiang, Emergent Haldane model and photon-valley locking in chiral cavities, [arXiv preprint arXiv:2403.11063](#) (2024).
- [27] Z. Bacciconi, H. Xavier, I. Carusotto, T. Chanda, and M. Dalmonte, Theory of fractional quantum Hall liquids coupled to quantum light and emergent graviton-polaritons, [arXiv preprint arXiv:2405.12292](#) (2024).
- [28] C. B. Dag and V. Rokaj, Engineering topology in graphene with chiral cavities, *Physical Review B* **110**, L121101 (2024).
- [29] D. Hagenmüller, J. Schachenmayer, S. Schütz, C. Genes, and G. Pupillo, Cavity-enhanced transport of charge, *Physical review letters* **119**, 223601 (2017).
- [30] N. Bartolo and C. Ciuti, Vacuum-dressed cavity magnetotransport of a two-dimensional electron gas, *Physical Review B* **98**, 205301 (2018).
- [31] D. Hagenmüller, S. Schütz, J. Schachenmayer, C. Genes, and G. Pupillo, Cavity-assisted mesoscopic transport of fermions: Coherent and dissipative dynamics, *Physical Review B* **97**, 205303 (2018).
- [32] G. Arwas and C. Ciuti, Quantum electron transport controlled by cavity vacuum fields, *Physical Review B* **107** (2023).
- [33] V. Rokaj, J. Wang, J. Sous, M. Penz, M. Ruggenthaler, and A. Rubio, Weakened topological protection of the quantum Hall effect in a cavity, *Physical Review Letters* **131**, 196602 (2023).
- [34] L. Winter and O. Zilberberg, Fractional quantum Hall edge polaritons, [arXiv preprint arXiv:2308.12146](#) (2023).
- [35] G. L. Paravicini-Bagliani, F. Appugliese, E. Richter, F. Valmorra, J. Keller, M. Beck, N. Bartolo, C. Rössler, T. Ihn, K. Ensslin, C. Ciuti, G. Scalari, and J. Faist, Magneto-transport controlled by Landau polariton states, *Nature Physics* **15**, 186 (2018).
- [36] F. Appugliese, J. Enkner, G. L. Paravicini-Bagliani, M. Beck, C. Reichl, W. Wegscheider, G. Scalari, C. Ciuti, and J. Faist, Breakdown of topological protection by cavity vacuum fields in the integer quantum Hall effect, *Science* **375**, 1030 (2022).
- [37] K. Kuroyama, J. Kwoen, Y. Arakawa, and K. Hirakawa, Electrical detection of ultrastrong coherent interaction between Terahertz fields and electrons using quantum point contacts, *Nano Letters* **23**, 11402 (2023).
- [38] K. Kuroyama, J. Kwoen, Y. Arakawa, and K. Hirakawa, Coherent interaction of a few-electron quantum dot with a Terahertz optical resonator, *Physical Review Letters* **132**, 066901 (2024).
- [39] J. Enkner, L. Graziotto, F. Appugliese, V. Rokaj, J. Wang, M. Ruggenthaler, C. Reichl, W. Wegscheider, A. Rubio, and J. Faist, Testing the renormalization of the von Klitzing constant by cavity vacuum fields, *Physical Review X* **14**, 021038 (2024).
- [40] J. Enkner, L. Graziotto, D. Boriçi, F. Appugliese, C. Reichl, G. Scalari, N. Regnault, W. Wegscheider, C. Ciuti, and J. Faist, Enhanced fractional quantum Hall gaps in a two-dimensional electron gas coupled to a hovering splitting resonator, [arXiv preprint arXiv:2405.18362](#) (2024).
- [41] G. Jarc, S. Y. Mathengattil, A. Montanaro, F. Giusti, E. M. Rigoni, R. Sergo, F. Fassoli, S. Winnerl, S. Dal Zilio, D. Mihailovic, P. Prelovšek, M. Eckstein, and D. Fausti, Cavity-mediated thermal control of metal-to-insulator transition in 1T-TaS₂, *Nature* **622**, 487–492 (2023).
- [42] S. Datta, *Electronic Transport in Mesoscopic Systems* (Cambridge University Press, 1995).
- [43] J.-P. Malrieu, P. Durand, and J.-P. Daudey, Intermediate Hamiltonians as a new class of effective Hamiltonians, *Journal of Physics A: Mathematical and General* **18**, 809 (1985).
- [44] R. Landauer, Spatial variation of currents and fields due to localized scatterers in metallic conduction, *IBM Journal of research and development* **1**, 223 (1957).
- [45] M. Büttiker, Four-terminal phase-coherent conductance, *Physical review letters* **57**, 1761 (1986).
- [46] D. S. Fisher and P. A. Lee, Relation between conductivity and transmission matrix, *Physical Review B* **23**, 6851 (1981).
- [47] L. P. Zárbo and B. K. Nikolić, Spatial distribution of local currents of massless Dirac fermions in quantum transport through graphene nanoribbons, *Europhysics Letters* **80**, 47001 (2007).
- [48] Y. Meir and N. S. Wingreen, Landauer formula for the current through an interacting electron region, *Physical Review Letters* **68**, 2512 (1992).
- [49] S. M. Girvin and K. Yang, *Modern Condensed Matter Physics* (Cambridge University Press, 2019).
- [50] J. Faist, Interchannel scattering and interior contacts in the quantum hall effect, *Europhysics Letters* **15**, 331 (1991).
- [51] The dimension of the dense (not sparse) Hamiltonian matrix in our case is $7'000 \times 7'000$, which is close to the memory limit in our computer cluster.
- [52] H. Van Houten and C. Beenakker, Quantum point contacts, *Physics today* **49**, 22 (1996).
- [53] Y. Aharonov and D. Bohm, Significance of electromagnetic potentials in the quantum theory, *Phys. Rev.* **115**, 485 (1959).
- [54] V. I. Puller and Y. Meir, Controlled breaking of phase symmetry in a “which-path?” interferometer, *Journal of Physics: Conference Series* **193**, 012011 (2009).